Journal of Materials Chemistry A

Accepted Manuscript

ROYAL SOCIETY OF CHEMISTRY

www.rsc.org/materialsA

One-Step In Situ Hydrothermal Fabrication of D/A Poly(3-hexylthiophene)/TiO_2 Hybrid Nanowires and Its Application in Photovoltaic Devices

Chi-Ju Chiang,[a] Yi-Huan Lee,[a] Yu-Ping Lee,[a] Guan-Ting Lin,[a] Ming-Hao Yang,[a] Leeyih Wang,[b] Chih-Chen Hsieh,[*,a] and Chi-An Dai[*,a]

[a]Department of Chemical Engineering and [b]Center for Condensed Matter Sciences, National Taiwan University, Taipei 10617, Taiwan

* Corresponding author: Chi-An Dai, Professor

Address: No. 1, Roosevelt Rd. Sec. 4, Department of Chemical Engineering, National Taiwan University, Taipei 10617, Taiwan

Phone No. 886-2-3366-3051, Fax No. 886-2-2362-3040, Email: polymer@ntu.edu.tw

* Corresponding author: Chih-Chen Hsieh, Associate Professor

Address: No. 1, Roosevelt Rd. Sec. 4, Department of Chemical Engineering, National Taiwan University, Taipei 10617, Taiwan

Phone No. 886-2-3366-3038, Fax No. 886-2-2362-3040, Email: ccjhsieh@ntu.edu.tw

Abstract:

In this study, we developed a novel *in situ* hydrothermal method to fabricate self-assembled P3HT/TiO_2 hybrid nanowires, wherein a facile one-step synthetic strategy was utilized to co-organize P3HT molecules and titanium precursors into highly elongated hybrid nanowires, followed by a hydrothermal process in an autoclave to *in situ* transform the titanium precursors into

crystalline TiO_2 nanoparticles on the P3HT nanofibrils. P3HT nanofibrils were utilized as a structure-directing motif to achieve a favorable dispersion of electron acceptor (A) TiO_2 nanocrystals of 10-15 nm in diameter embossed along the nanofibrils, as well as an efficient electron donor (D) for the nanohybrid. Particularly, the crystallization temperature of anatase-phase TiO_2 nanoparticles with high crystallinity via the hydrothermal method was significantly reduced to 130 °C in an elevated pressure of ~ 7 bars as compared to the conventional calcination temperature of 450 °C at ambient pressure for TiO_2 nanocrystal synthesis, therefore, allowing the synergistic one-step fabrication of both highly crystalline TiO_2 nanoparticles embossed on highly crystalline long-range ordered P3HT nanofibrils. As a consequence of the structural development, this P3HT/TiO_2 embossed nanohybrids could afford significant improvements in their D/A interfacial contact area for effective charge separation without the need of capping ligands typically used in ex-situ D/A blend systems, as well as efficient pathway for charge transport, leading to enhanced optoelectronic properties and device performance. The highest conversion efficiency of 0.14% was presented from the P3HT/TiO_2 embossed hybrid device, which was a remarkable improvement as compared to only 0.03% from an ex-situ P3HT/TiO_2 hybrid device. This novel *in situ* approach shows a feasible way to fabricate organic/inorganic nanohybrid materials of conjugated copolymers with different inorganic nanoparticles for the applications of future optoelectronic devices.

1. Introduction

The advance of organic/inorganic hybrid materials based on π-conjugated polymers and inorganic semiconductors has attracted great interests over the past decades due to its potential usage in optoelectronic applications such as light-emitting diodes, photodetectors, solar cells and others. In particular, significant consideration has been focused on the solution-processed hybrid solar cells consisting of electron-donating conducting polymers such as poly (3-hexyl thiophene) (P3HT) and electron-accepting nanocrystals (e.g., CdS, CdSe, ZnO, and TiO_2). While power conversion efficiencies (PCEs) for these hybrid bulk heterojunction (BHJ) solar cells are constantly being improved, they still suffer from structure control issues with the fine adjustment of electron donors/acceptors distribution. Efficient charge separation relies upon molecular interfaces to separate charge, and the domain size of the organic donor and inorganic acceptor materials should be comparable or smaller than the exciton diffusion length (~ 5-20 nm) to increase the probability of exciton dissociation across the donor-acceptor interfaces.[1] However, coagulation problems with inorganic nanocrystals often occur during the device fabrication process; that is, the blended organic/inorganic components may undergo macrophase separation that reduce the interfacial interactions between the polymer and inorganic materials, resulting in a decrease in the quantum efficiency, thereby degrading the device performance.[2] Consequently, controllable nanomorphology, well-structured interfaces, and superior optoelectronic interactions are critical factors for developing highly efficient hybrid solar cells.

To this end, a number of processing methodologies have been developed to achieve a high miscibility of organic/inorganic components and prepare a favorable dispersion of nanocrystals in hybrid photovoltaic devices. In a typical way, solubility of the nanocrystals can be achieved by using capping ligands, e.g. oleylamine, trioctylphosphite, 2-mercaptoethanol, but the modifying surfactants could be regarded as an isolating layer that hinder charge separation and charge transport.[3, 4] To overcome these drawbacks, it is necessary to remove excess capping ligands by additional procedures[5] or replace them with conjugated ones.[6, 7] Other routes also include the deposition of inorganic quantum dots on π-conjugated polymers via nanocrystal–polymer

interactions.[8] Prasad et al. designed a novel strategy by using thermally cleavable ligands to coat quantum dots, following a thermal annealing procedure on the as-fabricated photoactive layer to eliminate the ligands.[9] However, these methodologies often require complicated treatments, which could be too time-consuming to be applied to potential large-scale production.

An alternative strategy, which involves a π-conjugated polymer matrix such as P3HT containing a precursor of an inorganic component required for the synthesis of organic/inorganic nanohybrids, has recently received a great deal of attention on the fabrication of organic photovoltaic devices.[10] This is because the so-called "*in situ*" formation routes possess important advantages in that the effects of the capping ligands on charge exchange are eliminated and do not require a separate nanoparticle synthesis step, achieving direct combination of nanocrystals and polymer materials.[11] So far, a number of inorganic semiconductors (PbS, CdS, CdSe, ZnO and etc.) directly synthesized in conjugated polymers have been reported in several studies.[11-16] The correlation between the morphology, charge transport, and photovoltaic properties of the resulting BHJ systems has been also reported.[17-19] For the *in situ* synthetic process, developing a controllable morphology of nanohybrids and a well-defined interface between inorganic semiconductors and the conjugated polymers continues to be an important research topic. Our group previously reported a facile *in situ* method to fabricate highly elongated P3HT nanowires lined along their long fibril axis, with continuous ZnO nanocrystal pathways, where a "pre-crystallization" approach was first utilized to simultaneously organize organic P3HT molecules and inorganic zinc precursors into highly ordered nanowires with micrometer-scale lengths, followed by a thermal oxidation treatment to directly grow discrete ZnO nanocrystals on the existing nanofibrillar template at the ambient pressures.[20]

Despite continuous improvements in hybridization strategies, the *in situ* generation of metal oxide semiconductor inside the dry-state, π-conjugated polymer film remains suboptimal. Conversion and high crystallinity of inorganic semiconductors are strongly limited by the low annealing temperature used for the sake of preventing degradation of polymer components. Thus, the quality of nanocrystals as prepared is relatively poor, less crystalline than those produced from calcination or colloidal synthesis.[21, 22] Furthermore, only a few types of inorganic semiconductors

with high crystallinity could be prepared successfully below the decomposition temperature of polymers via *in situ* synthetic process, for instance, a high-temperature heating treatment above 450 °C is required to transform titanium precursors, such as titanium tetraisopropoxide (TTIP) or titanium tetrachloride ($TiCl_4$) into crystalline TiO_2.[23] However, TiO_2 as an electron acceptor for the use in photovoltaics has the advantages of resistance to acid and base, good chemical and photochemical stability, non-toxicity, low cost, and better charge separation properties.[24] These advantages have attracted intensive interest focusing on TiO_2.[24-29] Fortunately, hydrothermal synthetic technique provides a prospective route to prepare a well-crystalline and phase-pure oxide in one step in a tightly closed stainless steel autoclave under controlled temperatures ($T < 200$ °C) and/or pressures ($p < 10$ MPa).[30, 31] O'Regan and Grätzel synthesized anatase TiO_2 nanoparticles by hydothermal synthesis from titanium (IV) isopropoxide at 200 °C.[32] Imai et al. developed a new method of preparation of anatase TiO_2 films at low temperature by exposure to water vapor.[33, 34] Langlet et al. also reported on the possibility to crystallize TiO_2 thin films on polymer substrates and thermally sensitive substrates by using an autoclave under ethanol-water pressure.[35, 36] Besides, a high-pressure crystallization process developed by Lu's group has been utilized to successfully crystallize TiO_2 thin films at a temperature considerably lower than that required in a commonly adopted atmospheric pressure annealing process.[37] Therefore, the hydrothermal technique of TiO_2 preparation provides us with a practical approach to apply an *in situ* synthetic method for fabricating TiO_2/conjugated polymer nanohybrids with a controllable nanostructure.

Herein, we report on a novel *in situ* growth strategy to fabricate P3HT/TiO_2 nanohybrids, where a one-step approach was used to simultaneously organize organic P3HT chains and inorganic titanium precursors into highly-elongated nanofibrils, followed by the hydrothermal synthesis process at an elevated pressure in an autoclave to directly grow highly-crystallized TiO_2 nanoparticles on the existing P3HT nanofibrils. The TiO_2 embossed nanofibrillar structure provides enhanced interfacial area for charge separation as well as efficient pathways for charge transport, thereby enhancing optoelectronic properties and device performance. We believe that the current study offers a scalable and modular approach towards the co-assembly of disparate materials into

close association in hybrid systems.

2. Experimental Section

2.1 Synthesis of P3HT homopolymer

The conjugated P3HT homopolymer, P3HT56 (M_n of P3HT = 56,200 g/mol, and M_w/M_n = 1.48), used in this study was synthesized by using the Grignard metathesis polymerization method described previously in the literature.[38, 39] The detailed characterization of the synthesized polymer is listed in the Supporting Information section.

2.2 *In situ* synthesis of P3HT/TiO_2 nanohybrids with nanowire structure

TiO_2 nanocrystals were synthesized *in situ* on P3HT nanowires with the addition of TiO_2 precursor titanium (IV) tetraisopropoxide (TTIP) in the P3HT solution. The detailed synthesis procedure is listed as follows. First, P3HT56 homopolymer was added to chlorobenzene (CB) solution to prepare a 1.0 wt% solution at 60 ^oC, followed by the addition of TTIP (97.0% pure, Aldrich) to the P3HT/CB solution in different molar ratios of 3-hexylthiophene monomer units to Ti^{4+} (3HT/Ti^{4+}) of 1:0.33, 1:0.66, 1:1 and 1:2. After stirring for 2 days, nanowire assembly of the polymeric complexes was carried out via the addition of anisole, a poor solvent to P3HT, into the mixture to obtain a 0.5 wt% solution. This was followed by stirring for another day. Subsequently, the P3HT/inorganic hybrid complexes were spin-coated or drop-casted onto variant substrates, e.g. quartz pieces, silicon wafers, or copper grids. Then, the *in situ* growth of TiO_2 nanocrystals on P3HT nanowires were achieved by using an elevated pressure hydrothermal synthesis process on the coated film. In details, the coated polymer/complex thin film was first put into an enclosed stainless-steel autoclave with an inner chamber volume of 20 ml. A solution of ~ 3 ml of H_2O/MeOH in a beaker (1:1 vol%) had also been placed in the autoclave, followed by placing the enclosed autoclave inside an oven for heating. A high pressure, steam saturated environment was created by thermally heating the enclosed stainless-steel autoclave filled with deionized water and methanol at 130 ^oC. For different treatments presented hereafter, stable temperature and pressure were reached within ca. 30 mins. Autoclaving treatments were performed in a range of 2 to 9 h. After the hydrothermal treatment, the autoclave was rapidly opened in order to discharge the vapor and to avoid its condensation on the film surface,

followed by cooling down the samples to room temperature. During the hydrothermal process, the pressure inside the enclosed chamber was measured to be around 7.2 bars as indicated by a manometer pressure gauge. Finally, the resulting P3HT/TiO_2 hybrids with D/A (donor/acceptor) network nanowire structures were obtained by performing the above-mentioned high-pressure hydrothermal treatment.

2.3 Transmission electron microscopy (TEM)

To investigate the nanostructure and the embedded nanoparticle morphology of the P3HT/TiO_2 hybrids in the thin film state prepared by using the current *in situ* hydrothermal process, transmission electron microscopy (TEM) was employed. Samples for TEM measurements were prepared by depositing a droplet of the P3HT/inorganic hybrid complex solution onto a carbon-coated copper grid, followed by drying the sample in air for 6 h. Then, the P3HT/TiO_2 hybrid sample underwent the hydrothermal crystallization process. Bright field images were recorded on a JEOL 1230EX operating at 100 kV with a Gaten Dual Vision CCD Camera.

2.4 Grazing incidence small-angle and wide-angle X-ray scattering (GISAXS and GIWAXS)

Samples for X-ray scattering measurements were prepared by following the same sample preparation procedure for TEM, except that the coating was performed on silicon wafers instead of on copper grids. GISAXS and GIWAXS experiments were performed separately at the 23A1 and 17A1 endstations at the National Synchrotron Radiation Research Center (NSRRC) in Taiwan. The wavelength of the incident beam was 1.1809 Å for the GISAXS and 1.3213 Å for the GIWAXS measurements. For the GISAXS measurements, an incident angle of 0.2° was used, and the scattering patterns were collected on a Mar-CCD with a diameter of 165 mm. The one-dimensional scattering profiles along the q_{xy} axis (in-plane) were reported as plots of scattering intensity, I, versus the scattering vector, q. The scattering vector q was calibrated using a standard sample of Ag-behenate. For the GIWAXS measurements, the incident angle was set to 0.2° as well, and the scattering patterns were collected using a Mar3450 image plate detector. The two-dimensional

XRD patterns observed for the measured samples were also circularly averaged to obtain one-dimensional diffraction profiles along the q_{xy} and q_z axis (out-of-plane) as plots of the scattering intensity versus the scattering vector, with the value of q calibrated using standard samples of Ag-behenate and Si wafer.

2.5 Photophysical property analysis

The UV-VIS absorption measurements of the hybrid samples were conducted using a Cary 100 UV-visible spectrophotometer at room temperature. The thin film samples used in the analysis were prepared by coating hybrid samples on quartz pieces using the same sample preparation for the GIXS measurements. UV-VIS absorption was performed in a scanning range from 230 to 750 nm. The photoluminescence lifetimes spectra in the solid state were obtained by exciting film samples (~80 nm in thickness) at 478 nm monochromatic light with an average power of 1 mW, operating at 25 MHz in a duration of 70 ps. The PL signal was collected using a Pico Quant avalanche photodiode with the detection wavelength of 650 nm.

2.6 Solar Cell Device Fabrication and Characterization

Solar cells were fabricated with a so-called "inverse" device structure[19, 40, 41] of FTO/c-TiO_2/active layer/P3HT/PEDOT:PSS/Au. Fluorine-doped glass substrates (FTO) (Pilkington, 15 Ω/square) substrates were sequentially cleaned with deionized water, acetone, aqueous detergent, and isopropyl alcohol in an ultrasonic bath and then dried under N_2 flow. The cleaned FTO substrates were subsequently coated with a compact layer of TiO_2 (c-TiO_2) by aerosol spraying a precursor solution prepared by mixing titanium isopropoxide (0.284 g) and acetylacetone (0.203 g) in ethanol (5.0 mL), using air as the carrier gas. The film was then calcined at 450 ^oC for 30 mins under air, producing a dense TiO_2 layer with a thickness of around 80 nm. Then, P3HT/inorganic hybrid complexed from a CB solution was spin-coated onto the c-TiO_2 layer, followed by applying the hydrothermal crystallization process to obtain the active layer comprising of P3HT/TiO_2 hybrids with a D/A network structure. An additional pristine P3HT film was deposited on the top

P3HT/TiO_2 hybrid layer by spin-coating a solution of P3HT (45 mg/ml in chlorobenzene), which was followed immediately by a heat treatment performed at 150 °C for 10 mins. The pristine P3HT film was acted as a hole transport layer (HTL) at the direction toward the anode, thereby both increasing the charge collection efficiency and preventing the exciton recombination at the anode.[42] Poly(3,4-ethylenedioxythiophene):poly(styrene sulfonate) (PEDOT:PSS) was then spin coated onto the coated substrate at 3500 rpm, followed by annealing it at 120 °C for 6 mins in air. Finally, a cathode was then prepared by thermal evaporation of a layer of gold (100 nm thick) onto the coated samples. The solar cells were irradiated with simulated AM 1.5G (100 mW/cm^2) using a Newport 91160 W, a xenon-based lamp solar simulator. A Keithley 2400 electrometer was then used to evaluate the *J-V* characteristics of the solar cells.

3. Results and Discussion

3.1 Morphology and self-assembly behaviors

The hydrothermal process for the fabrication of P3HT/TiO_2 nanohybrid *in situ* under an elevated pressure is schematically illustrated in Scheme 1. This method starts with preparing a P3HT/Ti^{4+} complex solution by dissolving P3HT in chlorobenzene to obtain a 2.5 mg mL^{-1} (0.25 wt%) polymer solution, followed by mixing it with titanium tetraisopropoxide (TTIP) while keeping the amount of 3HT units to Ti^{4+} at the molar ratios of 1:0.33, 1:0.66, 1:1, and 1:2. For the P3HT/Ti^{4+} hybrid solution, the sulfur atom of the thiophene unit acted as an anchoring site for the coordination with titanium precursors. Subsequently, the nanofibril assembly of the polymeric complexes was carried out via the addition of anisole into the solution.[20] The addition of anisole, a poor solvent for P3HT, was found to induce a transition for the P3HT/Ti^{4+} complexes from a twisted coil-like micelle state to a more planar rod-like conformation, thereby resulting in a strong π-π interaction between P3HT chains, which served as the dominant driving force for molecular packing leading to highly ordered nanofibrillar structures with lengths on the order of micrometers. In the end, the titanium precursors were transformed into crystalline TiO_2 nanoparticles *in situ* on P3HT fibrils via the presence of H_2O/MeOH mixed vapor at an elevated pressure in an enclosed chamber heated at 130 °C for several hours. Consequently, TiO_2 nanocrystals were grown along the P3HT nanofibrillar template to form a 1-D embossed nanohybrid. In the current study, various lengths of the crystallization time were investigated at a fixed temperature of 130 °C during the hydrothermal synthesis process, and the obtained results were compared by GIWAXS measurements using a point-detector diffractometer. Fig. 1 shows the one-dimensional (along q_z axe) scattering patterns of the P3HT/TiO_2 thin film samples after various lengths of annealing time of the hydrothermal treatment. With 2 h of the treatment, only diffraction peaks corresponding to P3HT nanocrystals were detected, indicating that the titanium precursors remained mostly amorphous. When increasing the crystallization time to 6 h, TiO_2 nanocrystals were formed as illustrated in the corresponding XRD pattern in the enlarged inset figure in Fig. 1, in which all diffraction peaks are consistent with data characteristic of anatase TiO_2 crystals,[43, 44] indicating that a monophasic anatase-type TiO_2 was

obtained. This is because that the WAXS pattern of the hybrid sample exhibited diffraction peaks consisting of characteristic reflections of crystallographic planes of (101), (004), (200) and (211) associated with TiO_2 anatase nanocrystals. Note that the appearance of high order peaks of TiO_2 crystalline phase confirmed that the hydrothermal process at elevated pressure induced TiO_2 nanoparticles with high crystallinity. Meanwhile, the crystalline peaks, $(h00)_{P3HT}$ of P3HT become more intense, revealing synergistic effect that the P3HT nanofibrils also had a higher crystallinity after hydrothermal treatment. With a further increase in the crystallization time to 9 h, the diffraction peaks had no apparent change in the pattern of the nanohybrid for both P3HT and TiO_2 nanocrystals compared with those for samples with the 6 h treatment time, suggesting that the growth of TiO_2 nanoparticles had reached their plateau status at 6 h of hydrothermal treatment. In addition, from their full width at half maximum (FWHM) corresponding to anatase TiO_2 (101) peak, it can be observed that the FWHM of the TiO_2 (101) peak at 6 h was narrower than that at 2 h, indicating that the grain size of TiO_2 nanocrystals was larger with an increasing crystallization time at 6 h based on the analysis using Scherrer's equation.[45] In other words, it means that amorphous TiO_2 did not crystallize completely at the reaction time of only 2 h. However, as the reaction time was extended to 9 h, the grain size of TiO_2 nanocrystals estimated to be around 10 nm based on the XRD results was almost the same as that for the 6 h samples, suggesting that nearly all amorphous TiO_2 had crystallized into anatase TiO_2. Thus, it is suitable to use the optimized parameters for the hydrothermal synthesis process at 130 °C for 6 h. The results demonstrate that the crystallization temperature of anatase-phase TiO_2 nanocrystals could be significantly lowered under the high pressure hydrothermal process as compared to the conventional crystallization temperature of ~450 °C under the atmospheric pressure condition. In addition, the XRD results indicate that a nearly full conversion of TiO_2 and the estimated weight percentage of TiO_2 in the hybrid films is around 10%, 21%, 32%, and 64% for the films with initial 3HT/Ti^{4+}molar ratios corresponding to 1:0.33, 1:0.66, 1:1, and 1:2, respectively.

The morphology and self-assembly behavior of the P3HT/TiO_2 nanohybrids were characterized by using bright-field transmission electron microscopy (TEM). As a comparison, Fig. 2(a) shows a

TEM image of P3HT nanofibrils loaded with no titanium precursors prepared by drop casting the P3HT solution onto a carbon-coated copper grid, followed by the hydrothermal process. From the TEM image, we observed that the nanofibrils are well dispersed with an average fibril width of roughly 12-15 nm. The formation of the nanofibril nanostructure was predominantly driven by the strong rod-rod interactions between P3HT chains, thereby inducing P3HTs to self-organize into highly continuous nanofibrils or so-called nanowires. Next, the hybrid samples comprising the inorganic nanoparticles and polymer component were then also investigated by TEM. TEM images of P3HT/TiO_2 nanohybrid samples with variant molar ratios between 3HT units and Ti^{4+} ions are displayed in Fig. 2(b)-Fig. 2(d). The P3HT/TiO_2 hybrid samples were also prepared by depositing a droplet of the P3HT/inorganic hybrid complexes solution onto a carbon-coated copper grid, followed by using the hydrothermal process to obtain the P3HT/TiO_2 nanohybrids. Fig. 2(b) reveals the hybrid sample with the lowest TiO_2 content (3HT/TiO_2 = 1:0.33), where it was observed that the TiO_2 nanocrystals were grown sporadically along the P3HT nanowire template to form an organic/inorganic hybrid nanowire. In brief, the TiO_2 nanocrystals had been synthesized via the sol-gel method from the hydrolysis of the titanium precursor with the high pressure vapor of H_2O/MeOH diffusing into the film of P3HT/titanium (IV) alkoxide hybrid complexes, followed by a condensation reaction to form TiO_2 nanostructures.[46] There was no apparent change in the morphology of the polymer nanowires before and after the hydrothermal treatment, indicating that the growth of TiO_2 nanoparticles did not perturb the P3HT's self-assembly behavior attributed to the sulfur atoms of the P3HT molecules that were used as anchoring sites for coordination with titanium precursors. For the P3HT/TiO_2 sample with 3HT/TiO_2 = 1:1, its bright-field TEM micrograph (Fig. 2(c)) shows an embossed nanowire structure, in which the TiO_2 nanocrystals were predominately associated with P3HT fibrils rather than scattered around in the interstitial empty space where no P3HT nanofibril was present, indicating that the TiO_2 nanocrystals could be nucleated *in situ* from P3HT/Ti^{4+} chelated sites, followed by the growth of TiO_2 nanocrystals lining uniformly and compactly along the P3HT nanowire templates. Notably, the characteristic width of the nanofibrils in the TEM images progressively increased from ~12 to ~22 nm upon hydrothermal treatment of the

hybrid samples. This implies that the high pressure hydrothermal treatment significantly induced finer molecular packing in the hybrid films, leading to highly-crystallized structures with more extended chain conformations of P3HT as Ti^{4+} chelated ions formed TiO_2 nanocrystals and were expelled from the grown P3HT nanofibrils. This TEM results for the changes in P3HT nanofibril width are also consistent with the GIWAXS results shown in Fig. 1. As the amount of incorporated TiO_2 nanoparticles increased to a loading ratio of 3HT/TiO_2 = 1:2, the morphology of the hybrid system (Fig. 2(d)) with nanowire structure over very long distances remained unchanged. However, there were some TiO_2 nanocrystals dispersed within the interstitial spaces where no polymer was associated with them, revealing that some extra TiO_2 nanocrystals were migrating from the P3HT nanowire templates even though the remaining TiO_2 nanocrystals did not appear to deteriorate the P3HT's nanowire structure at this high loading of inorganic nanocrystals.

GISAXS measurements were subsequently carried out to identify changes in the thin film's morphology and internal structure. Shown in Fig. 3(a), 3(b), and 3(c) are the two-dimensional scattering profiles of the pristine P3HT after hydrothermal treatment and the P3HT/TiO_2 nanohybrid samples with 3HT/TiO_2 ratios of 1:1 and 1:2, respectively. For the pristine P3HT sample, the corresponding one-dimensional intensity profiles plotted versus the in-plane scattering vector, q_{xy}, showed that there was a shallow but visible scattering peak (indicated by an arrow) being exhibited in curve (iii) of Fig. 3(d). A calculation for the diameter of the nanowires based on this scattering peak position (q^*) gave a characteristic structural spacing of around 14.1 nm, which is close to the value for the nanofibril width measured from TEM images of 12-15 nm. From the one-dimensional SAXS spectra shown in the top two curves (i) and (ii) in Fig. 3(d), it was further observed that upon increasing TiO_2 nanocrystals loading, their characteristic scattering peaks in the GISAXS patterns became more distinct and moved to a lower q_{xy}. Therefore, the synergistic co-assembled P3HT/TiO2 hybrid nanofibrils become more ordered and the corresponding d-spacing progressively increased from 14.1 to 22.8 nm, which again was very similar to the results obtained from the TEM observations for the corresponding hybrid samples. The increased diameter of the nanowires is a strong evidence that the high pressure treatment significantly enhanced the P3HT to re-organize into

highly-crystalline structures with more extended chain conformations. Additionally, there was a simultaneous increase in the scattering peak intensity of the P3HT/TiO_2 hybrid samples, indicating an enhanced electron density contrast as a result of the nanoscale dispersion of TiO_2 nanocrystals embossed in the P3HT long-ranged nanowires which formed a D/A network structure.

3.2 Molecular packing of P3HT and TiO_2 in nanodomains

In order to further characterize the evolution of crystalline structure and molecular orientation of the hybrid system as a function of TiO_2 content, two-dimensional GIWAXS measurements were carried out. Shown in Fig. 4(a), (b), (c), and (d) are the two-dimensional X-ray scattering profiles of the P3HT/TiO_2 samples with 3HT/Ti molar ratios of 1:0.33, 1:0.66, 1:1, and 1:2, respectively. The corresponding one-dimensional intensity profiles along the q_z and q_{xy} axes of these four measured samples were also plotted as a function of scattering intensity versus the scattering vector, shown in Fig. 4(e) and (f). For these P3HT/TiO_2 hybrid samples, their corresponding GIWAXS patterns show an intense arcs of the $(h00)_{P3HT}$ layers along the q_z (substrate normal) axis. The $(020)_{P3HT}$ reflection located at q = 1.66 $Å^{-1}$ along the q_{xy} (substrate parallel) axis was also observed for all the hybrid samples except the sample with the highest nanoparticle loading of 3HT/Ti ratio of 1:2. The GIWAXS patterns showing oriented $(h00)_{P3HT}$ and $(020)_{P3HT}$ arcs demonstrate that the molecular packing of P3HT has highly ordered edge-on hexyl side chains, and that the π-conjugated planes of P3HT are parallel with respect to the substrate. The rest of the diffraction rings shown at higher scattering vectors can be referred to as the (101) and (004) planes, corresponding to the anatase form of TiO_2 nanocrystals. Note that the appearance of high order peaks of TiO_2 crystalline phase confirmed a high crystallinity of the high pressure hydrothermal process induced TiO_2 nanoparticles. Upon increasing the TiO_2 content, the WAXS patterns exhibited progressively increasing intensities of the TiO_2 signals, but with similar P3HT diffraction peak intensity. The presence of these structural features reflected the fact that the molecular packing of the P3HT component in the hybrid samples was not significantly disrupted by the addition of TiO_2 nanocrystals, consistent with the results from the TEM measurements. Through a combination of the TEM and 2D-GIWAXS structural

investigations, it can be concluded that the current *in situ* methodology provided an effective pathway to directly co-assemble highly-crystallized TiO_2 nanoparticles into well-ordered and long-ranged P3HT nanofibrils. Furthermore, this methodology carries advantages over a randomly distributed hybrid system, since macrophase segregation between organic P3HT nanofibrils and inorganic TiO_2 nanoparticles is minimized and the P3HT/TiO_2 interfacial contact area is maximized, and thus can be expected to enhance the exciton dissociation and charge transport, thereby improving optoelectronic properties and device performance. Following this promising strategy, a detailed study of the photophysical properties and photovoltaic application of the hybrid system is presented as follows.

3.3 Photophysical properties of P3HT/TiO_2 nanohybrids

The photophysical properties of the P3HT/TiO_2 nanohyrbids were explored by the thin-film UV-VIS absorption measurements. Fig. 5(a) shows the representative UV-VIS absorption spectra of the hybrid samples as a function of different nanoparticle loadings. These profiles have been normalized by the intensity of photons absorbed at 519 nm. For the P3HT/TiO_2 sample (3HT/TiO_2 = 1:0.33) treated by the hydrothermal crystallization process, its absorption spectrum gave an absorption maxima at 559 nm with two shoulders at 519 and 606 nm, which correspond to the vibronic splitting of the P3HT chromophore. The spectrum also showed an appearance of an absorption feature located at 360 nm, indicating the absorbance of TiO_2 nanocrystals. Upon increasing TiO_2 loadings, the TiO_2 absorbance showed a progressive increase while the absorption feature for the P3HT did not change significantly. These observations clearly indicate that the P3HT molecular packing could be highly crystalline after the high pressure hydrothermal treatment, and the co-assembly of TiO_2 nanoparticles did not appear to perturb the polymer self-assembly nanostructure. Overall, the high pressure induced P3HT/TiO_2 hybrid system showed a superior structural stability. As a result, the absorption spectra provide an insight viewpoint into the P3HT/TiO_2 nanohybrids and assure the photophysical property correlating well with the structural results from TEM and GIWAXS measurements.

Photoluminescence (PL) measurements were also conducted to analyze the efficiency of exciton dissociation and charge generation of the P3HT/TiO_2 hybrid samples. The PL spectra of the hybrid samples with different molar ratio of 3HT units to TiO_2, compared with pristine P3HT homopolymer are shown in Fig. 5(b). A broad emission band present around 600-750 nm occurred as a result of the P3HT film's optical excitation at 550 nm. In comparison with the emission of the pristine P3HT sample, the PL intensity is reduced by 50% for the hybrid (3HT/TiO_2 = 1:0.33), while a 90% reduction is seen for the nanohybrid with highest TiO_2 incorporation (3HT/TiO_2 = 1:2). This substantial reduction in the P3HT fluorescence could be ascribed to the efficient charge transfer from the P3HT chains to the TiO_2 nanocrystals. In order to provide additional information on the charge transfer dynamics in the P3HT/TiO_2 nanohybrids, time-resolved PL measurements (TRPL) were also conducted by exciting thin film samples at 478 nm monochromatic light, followed by the measurements of the fluorescence lifetime using a time-correlated single-photon counting (TCSPC) system. For the TRPL spectra with variant TiO_2 loading as shown in Fig. 6(a), the biexponential decay can be associated with a two-step process, wherein the fast decay component can be ascribed to the time of exciton separation (τ) at the interface between P3HT and TiO_2, and the slow decay component is due to the exciton-hole recombination time of P3HT. For the pristine P3HT, its exciton lifetime (τ) was measured to be around 146 ps. This value for the pristine P3HT is low compared with those obtained from other studies in those cases P3HT films with moderate or low crystallinity were often prepared, leading to a change in the exciton decay dynamics such that a single and larger exciton decay lifetime was obtained.[27, 47] For the pure and highly crystalline P3HT films, our result for exciton lifetime is found to be consistent with those from a recent study in which highly crystalline P3HT film was also used, resulting in the lifetime to be in the similar range of ~140 ps.[48-50] In addition, the hybrid sample with 3HT/TiO_2 = 1:0.33 exhibited an even shorter fluorescence lifetime (τ = 126 ps) than that of the P3HT homopolymer. It is apparent that the addition of TiO_2 nanocrystals resulted in a significant reduction in the photoluminescence lifetime. After increasing TiO_2 loading from 3HT/TiO_2 = 1:0.33 to 1:0.66 and finally to 1:1, the PL decay spectra revealed that the luminescence of the nanohybrids (1:0.66 and 1:1) had a lifetime of 121 ps and 115 ps,

respectively. As the incorporation of TiO_2 further increased to a ratio of 3HT/TiO_2 = 1:2, the fluorescence lifetime of the composite reached its lowest value of τ = 108 ps, indicating that the excitons in the sample were even more efficiently dissociated into charge carriers than that of the other samples. Taking these fluorescence results together, the photoluminescent features can be understood as follows: the synergistic co-assembled TiO_2 embossed nanowire structure provided intimate contact between p-type P3HT and n-type TiO_2 nanocrystals, and created a large amount of interfaces for charge dissociation, which results in a shorter PL lifetime, quenched PL intensities, and increased charge transfer rates. Fig. 6(b) shows the energy-level diagram of the P3HT/TiO_2 hybrid. The band energy levels of P3HT[51] and TiO_2[52] were obtained from the literature. From the energy-level diagram, it can be demonstrated that photoinduced charge transfer from the excited P3HT segments to the incorporated TiO_2 nanoparticles, and the following hole and electron carrier transport, is energetically favored. Thus, in the P3HT/TiO_2 hybrid system, a large-scale organic/inorganic coaxial nanowire structure imparts continuous, highly ordered nanochannels for a high electron donor/acceptor interfacial area, resulting in a more efficient photogenerated exciton dissociation and charge transport ability.

3.4 Device performance

As shown in Fig. 7(a), a structure of glass/FTO/c-TiO_2/active layer/P3HT/PEDOT:PSS/Au was referenced to produce photovoltaic devices from P3HT/TiO_2 hybrids. The current-voltage (*J–V*) characteristics of the photovoltaic devices illuminated under simulated AM 1.5 (100 mW/cm^2) conditions is shown in Fig. 7(b). Additionally, the photovoltaic parameters of these devices were summarized in Table S1. For the ex-situ P3HT/TiO_2 hybrid system (3HT/TiO_2 = 1:1), the device exhibited an open-circuit voltage (V_{oc}) of 0.488 ± 0.013 V, a short-circuit current density (J_{sc}) of 0.164 ± 0.036 mA/cm^2, a fill factor (FF) of 36.81 ± 4.64%, and gave a best power conversion efficiency (PCE_{best}) of 0.03%. This insufficient performance resulting from a low current density and a poor fill factor may be attributed to the occurrence of a partial macrophase separation of the P3HT/TiO_2 hybrid. When the *in situ* P3HT/TiO_2 embossed nanowire hybrid was used as active layer

(3HT/TiO_2 = 1:1), a significant improvement in the photovoltaic performance was achieved, giving an improved V_{oc} of 0.574 ± 0.023 V, J_{sc} of 0.412 ± 0.046 mA/cm^2, FF of 48.94 ± 4.29%, and PCE_{best} of 0.14%. This increase in the device performance could be regarded as an important signature of developing a well-defined interface between inorganic semiconductors and the conjugated polymers of high crystallinity in the *in situ* P3HT/TiO_2 hybrid film, whose existence was investigated by the TEM and X-ray measurements discussed above. When compared with the ex-situ P3HT/TiO_2 hybrid device, the efficiency achieved was approximately a 4.67 times improvement. Considering the significant quenching effect observed from our fluorescence studies, it is not surprising that the P3HT/TiO_2 embossed nanowire hybrid system exhibited a synergistic improvement on photovoltaic performance. The superior device performance was attributed to the pronounced structural improvement of the P3HT/TiO_2 morphology, *i.e.* the highly extended nanowires of P3HT and highly crystalline TiO_2 domains penetrating through a large portion of the device fabricated from the *in situ* hydrothermal crystallization process not only greatly promoted the D/A interfacial area for exciton separation, but also facilitated charge carrier transport and thus reduced possible recombination, leading to the superior J_{sc}, FF, and PCE of the device. As the amount of incorporated TiO_2 nanoparticles increased to a ratio of 3HT/TiO_2 = 1:2, the J_{sc} (0.552 ± 0.034 mA/cm^2) of the hybrid solar cell was apparently larger than those of the other two hybrid solar cells, revealing that the higher amount of TiO_2 nanocrystals constructed much more continuous percolation pathways for electron transport. However, the V_{oc} (0.430 ± 0.014 V) and FF (39.87 ± 3.08%) of the the hybrid solar cell was much lower than those of the other two hybrid solar cells, which translates to a power conversion efficiency of 0.11%, slightly lower than those of the P3HT/TiO_2 device with fewer TiO_2 content.

4. Conclusions

In summary, we have developed a novel and effective *in situ* strategy to cooperatively self-assemble TiO_2 nanocrystals embossed onto elongated P3HT nanowires to yield a nanohybrid with a highly ordered donor/acceptor (D/A) nanofibrillar structure that exhibited enhanced

optoelectronic properties. A pre-crystallization approach was used to simultaneously organize organic P3HT chains and inorganic titanium precursors into highly-elongated hybrid nanofibrils, where the sulfur atoms of the P3HT molecules were used to act as anchoring sites for the coordination of the titanium precursors. Subsequently, a high-pressure hydrothermal crystallization process can be used to *in situ* transform titanium precursors into crystalline TiO_2 nanoparticles on the existing P3HT nanofibrils. Notably, the crystallization temperature of anatase-phase TiO_2 nanocrystals was significantly reduced down to 130 °C in high pressures as compared to the conventional atmospheric pressure crystallization temperature at ~450 °C for the nanoparticle synthesis. By a combination of TEM, GISAXS and GIWAXS structural investigations, the detailed structural features and morphological changes of the P3HT/TiO_2 hybrid samples with various amount of TiO_2 loading were explored. Additionally, UV-VIS, PL, and TRPL measurements were used to investigate the optoelectronic properties of these hybrid samples. Based on these analyses, enhanced vibronic absorption, PL quenching, and shorter exciton lifetime were observed, indicating that excitons in the P3HT/TiO_2 embossed hybrid samples were efficiently dissociated into charge carriers. The TiO_2 embossed nanofibrillar structure provides enhanced interfacial area for charge separation as well as an efficient pathway for charge transport, thereby enhancing optoelectronic properties and device performance. The highest conversion efficiency of 0.14% was obtained from the P3HT/TiO_2 embossed hybrid device with a 3HT/TiO_2 ratio of 1:1, which was approximately a 4.67 times improvement compared with the ex-situ P3HT/TiO_2 hybrid device. We believe that the *in situ* conjugated polymer/inorganic nanoparticles embossed hybrid material shows potential for use in future optoelectronic applications.

5. Acknowledgements

The financial support under grants MOST 103-2221-E-002-281-MY3 from the Ministry of Science and Technology of Taiwan is greatly appreciated. The X-ray measurements were conducted at National Synchrotron Radiation Research Center (NSRRC) in Taiwan. The authors would also like to thank Dr. Ming-Tao Lee and Dr. Jey-Jau Lee for their help during the X-ray experiments.

6. Appendix A. Supporting information

Detailed synthesis procedures and characterization data (GPC and device performance) of the polymer samples. This material is available free of charge via the Internet at http://dx.doi.org/10.1039/

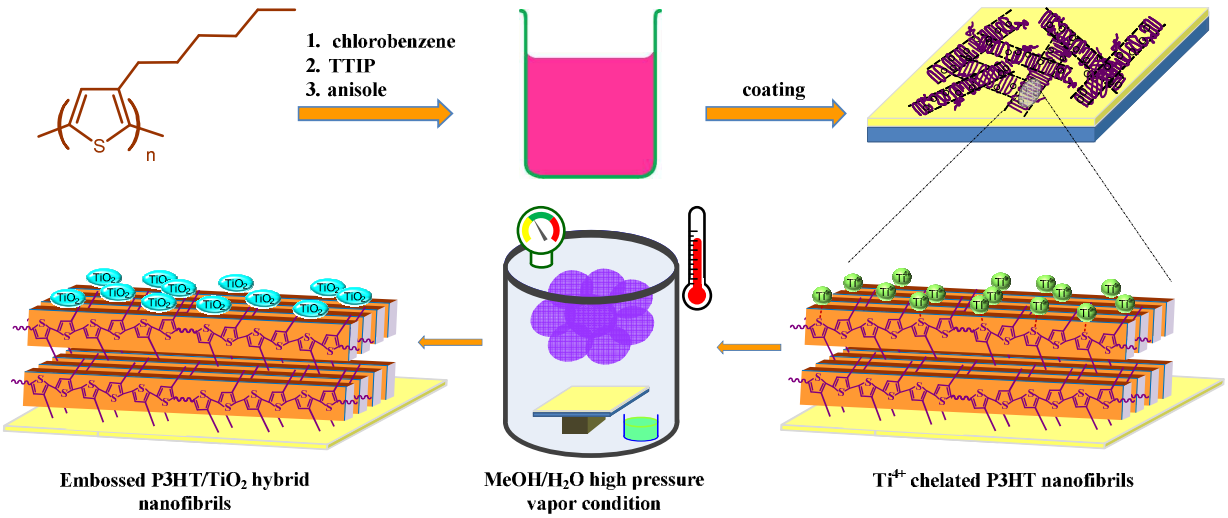

Scheme 1 Reaction scheme for the formation of *in situ* nanohybrid containing TiO_2 nanoparticles decorated P3HT nanofibrils via the high-pressure hydrothermal crystallization process.

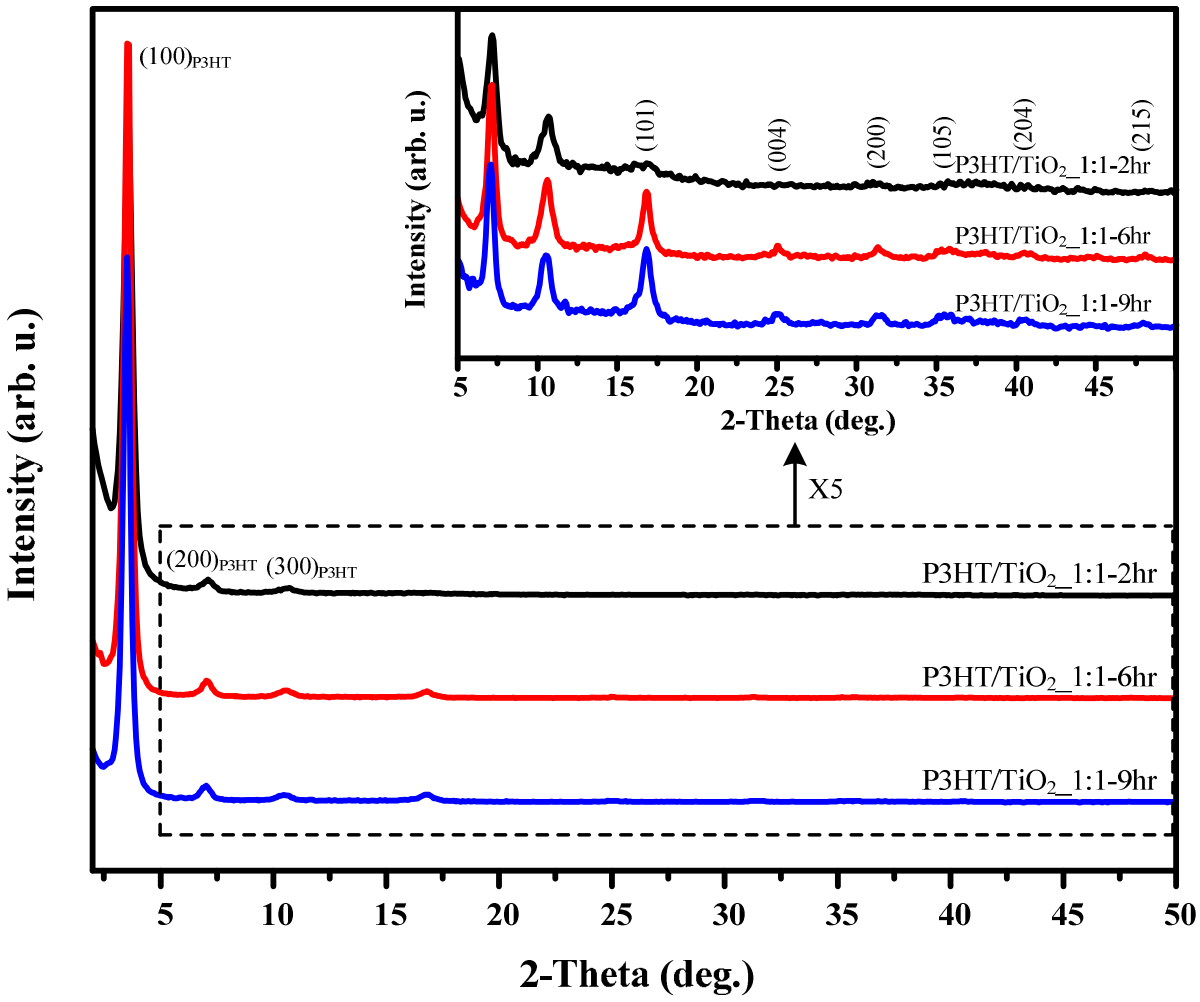

Fig. 1 The WAXS spectra of solvent-cast P3HT/TiO_2 (with a fixed TiO_2 content 3HT/TiO_2 = 1:1) hybrid thin film samples after various lengths of annealing time during the hydrothermal crystallization process, i.e., 2 h, 6h, and 9 h, respectively at 130 ^oC. The inset picture shows the XRD profiles of the corresponding P3HT/TiO_2 hybrid samples magnified by 5 times.

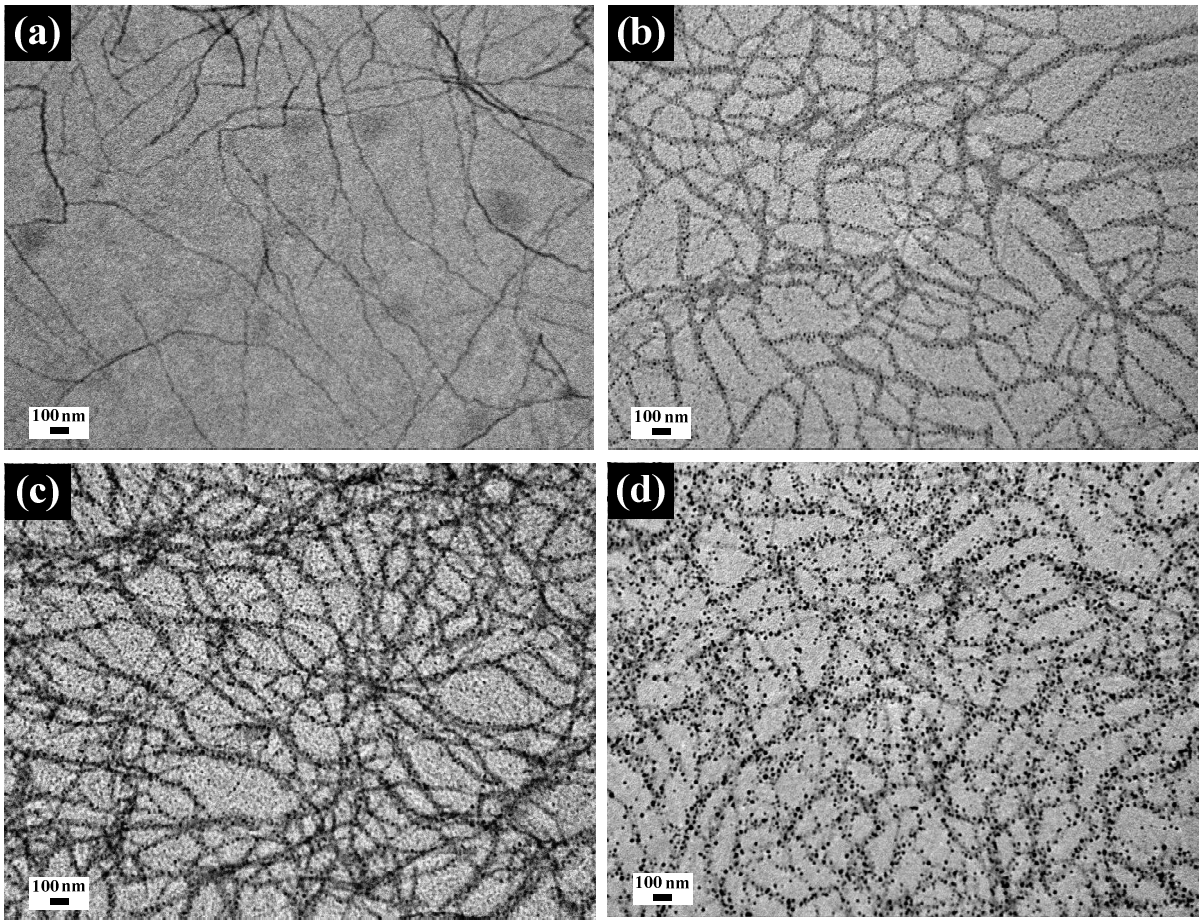

Fig. 2 TEM images of drop-cast samples of the nanofibrillar structures of (a) pristine P3HT, (b) P3HT/TiO_2 hybrid with 3HT/TiO_2 = 1:0.33, (c) P3HT/TiO_2 hybrid with 3HT/TiO_2 = 1:1 and (d) P3HT/TiO_2 hybrid with 3HT/TiO_2 = 1:2. All of the above samples were prepared via the hydrothermal crystallization process.

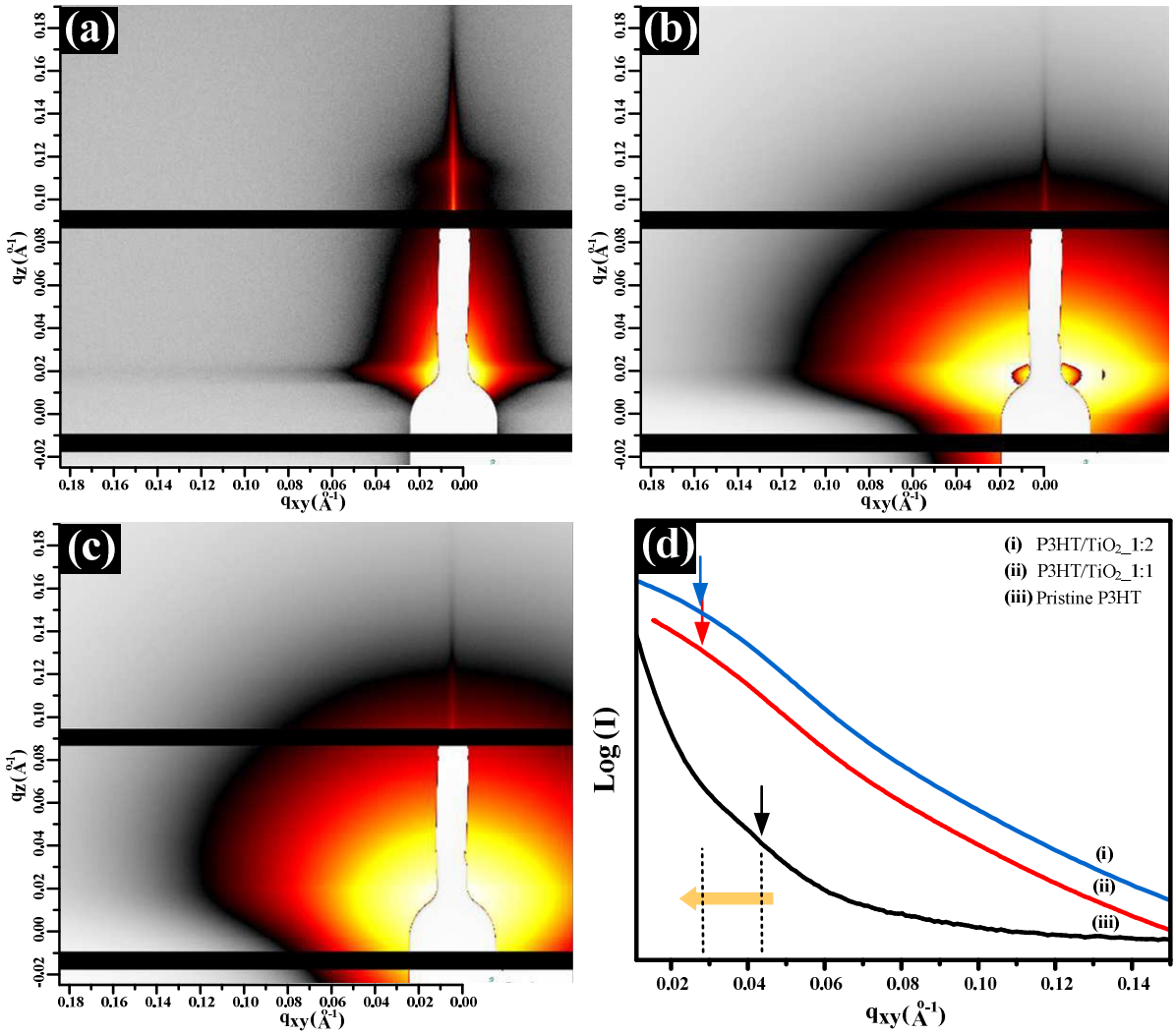

Fig. 3 Two-dimensional GISAXS scattering patterns of thin films of (a) pristine P3HT, (b) P3HT/TiO_2 hybrid with 3HT/TiO_2 = 1:1, and (c) P3HT/TiO_2 hybrid with 3HT/TiO_2 = 1:2 samples. For the GISAXS measurements, an incident angle of 0.2° was used. To obtain statistically averaged information on the internal structure of these thin film samples, the corresponding one-dimensional scattering spectra in the horizontal direction (d) of the above three images were taken. The arrows indicate the scattering peaks associated with the structural characteristics of these samples' nanofibrils.

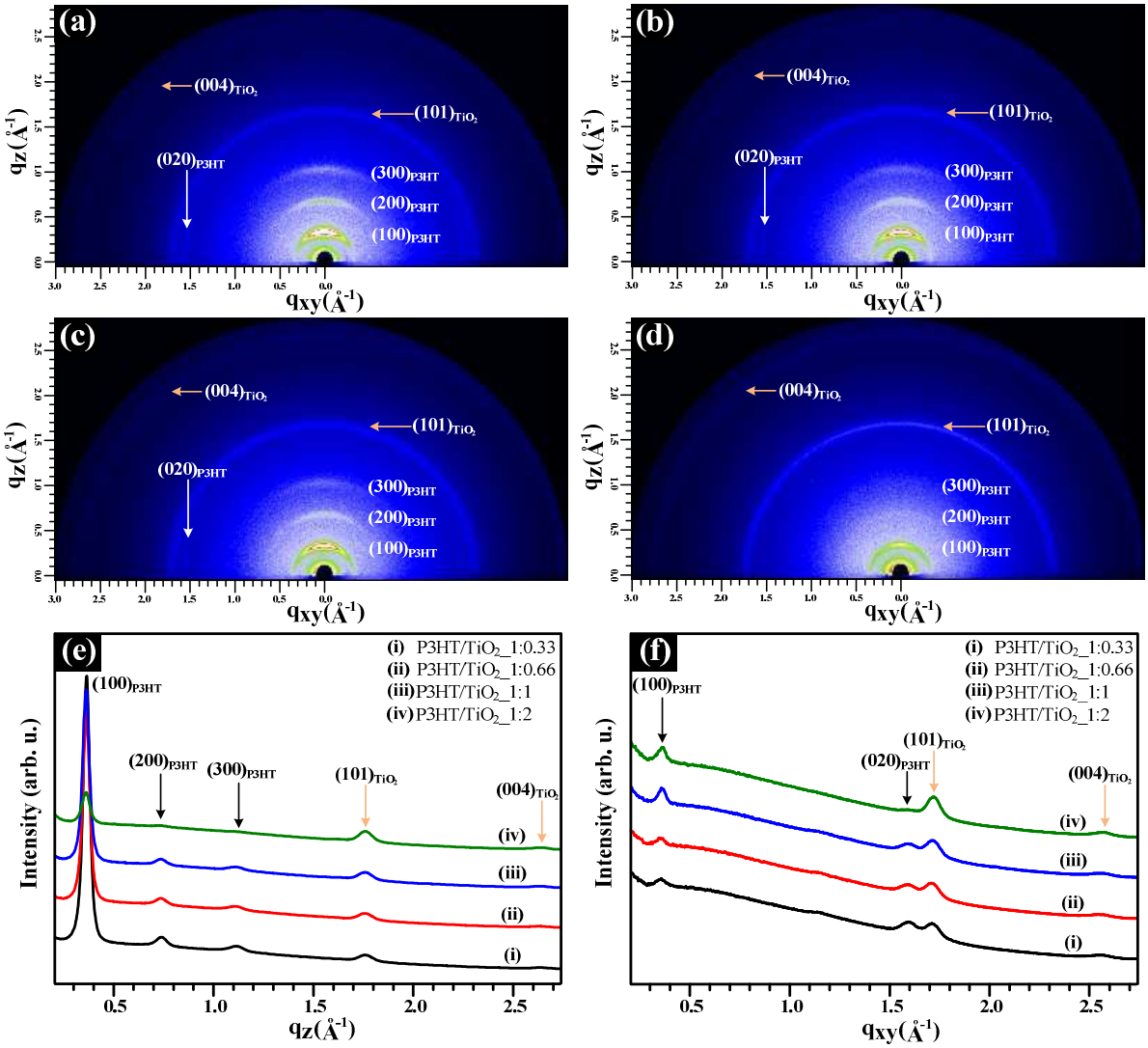

Fig. 4 Two-dimensional GIWAXS scattering spectra of (a) P3HT/TiO_2 hybrid with 3HT/TiO_2 = 1:0.33, (b) P3HT/TiO_2 hybrid with 3HT/TiO_2 = 1:0.66, (c) P3HT/TiO_2 hybrid with 3HT/TiO_2 = 1:1 and (d) P3HT/TiO_2 hybrid with 3HT/TiO_2 = 1:2. The corresponding one-dimensional GIWAXS profiles along *qz*, and *qxy* axis were extracted for the four samples, as shown in (e) and (f), respectively.

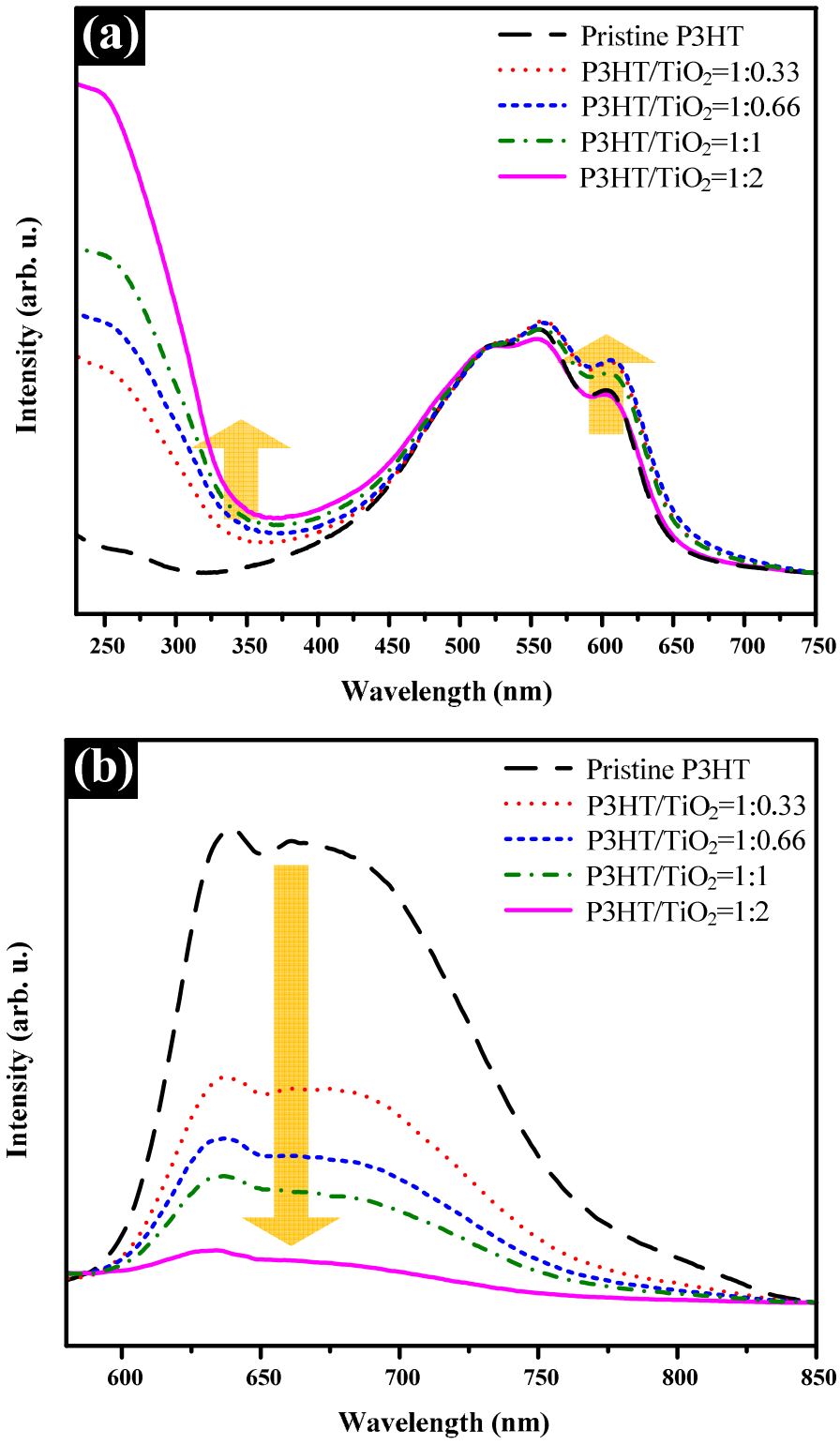

Fig. 5 (a) UV-VIS and (b) PL spectra of pristine P3HT and the *in situ* grown P3HT/TiO_2 hybrid samples with different molar ratio of 3HT monomer units to TiO_2 by exciting the tested samples at 550 nm.

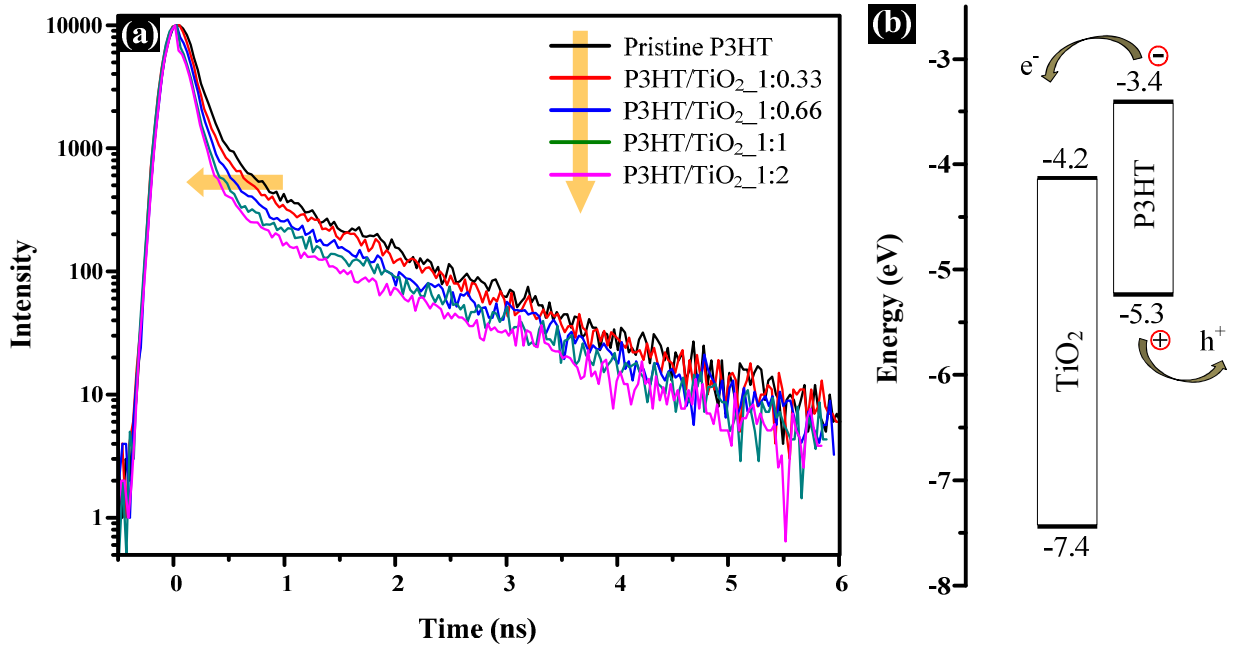

Fig. 6 (a) Time-resolved photoluminescence spectra of pristine P3HT and the P3HT/TiO_2 hybrid samples with different molar ratios of 3HT units to TiO_2 by exciting the samples at 478 nm of monochromic light. (b) The energy-level diagram for the co-assembled P3HT/TiO_2 hybrid D/A network system.

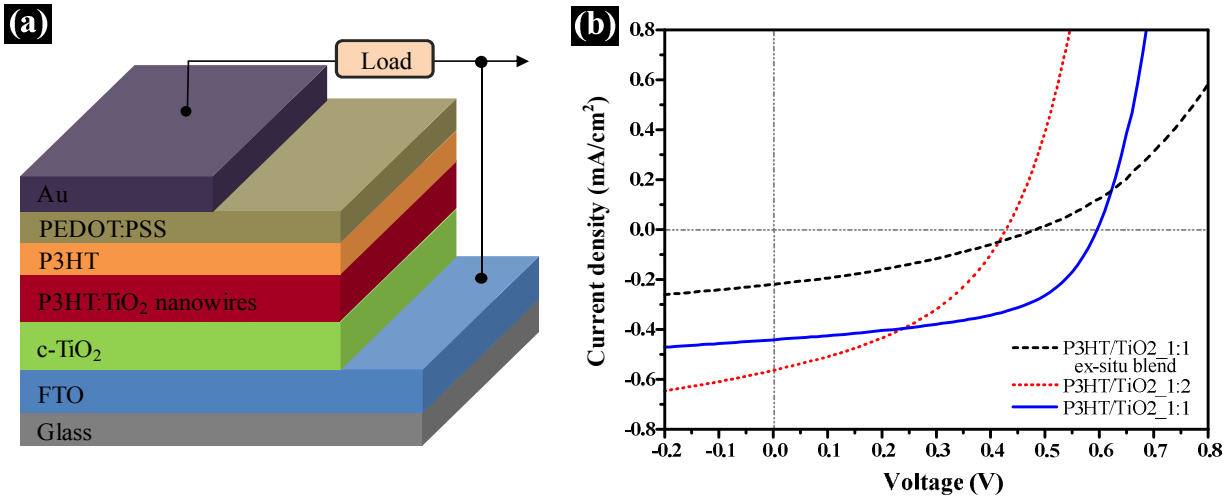

Fig. 7 (a) Schematic illustration showing the architecture of a photovoltaic device. (b) Current density-voltage (*J-V*) characteristics of the P3HT/TiO_2 hybrid based photovoltaic devices under 100 mW/cm^2 AM 1.5G solar irradiation.

References:

1. S. Ren, L.-Y. Chang, S.-K. Lim, J. Zhao, M. Smith, N. Zhao, V. Bulović, M. Bawendi and S. Gradečak, *Nano Lett.*, 2011, **11**, 3998-4002.
2. W. J. E. Beek, M. M. Wienk and R. A. J. Janssen, *Adv. Mater.*, 2004, **16**, 1009-1013.
3. T. Rath, M. Edler, W. Haas, A. Fischereder, S. Moscher, A. Schenk, R. Trattnig, M. Sezen, G. Mauthner, A. Pein, D. Meischler, K. Bartl, R. Saf, N. Bansal, S. A. Haque, F. Hofer, E. J. W. List and G. Trimmel, *Adv. Energy Mater.*, 2011, **1**, 1046-1050.
4. Y.-H. Lee, Y.-P. Lee, C.-J. Chiang, F.-K. Wei, C.-H. Wu, W.-C. Chen, C. Shen, H.-A. Jeng, L. Wang, M.-W. Liu, Y.-F. Chen, T. Yokozawa and C.-A. Dai, *J. Mater. Chem. A*, 2014, **2**, 14600-14612.
5. Y. Zhou, F. S. Riehle, Y. Yuan, H.-F. Schleiermacher, M. Niggemann, G. A. Urban and M. Krüger, *Appl. Phys. Lett.*, 2010, **96**, 013304.
6. F. A. Bokel, P. K. Sudeep, E. Pentzer, T. Emrick and R. C. Hayward, *Macromolecules*, 2011, **44**, 1768-1770.
7. E. B. Pentzer, F. A. Bokel, R. C. Hayward and T. Emrick, *Adv. Mater.*, 2012, **24**, 2254-2258.
8. J. Xu, J. Hu, X. Liu, X. Qiu and Z. Wei, *Macromol. Rapid Commun.*, 2009, **30**, 1419-1423.
9. J. Seo, W. J. Kim, S. J. Kim, K.-S. Lee, A. N. Cartwright and P. N. Prasad, *Appl. Phys. Lett.*, 2009, **94**, 133302.
10. Y. Peng, G. Song, X. Hu, G. He, Z. Chen, X. Xu and J. Hu, *Nanoscale Res. Lett.*, 2013, **8**, 106.
11. S. Dayal, N. Kopidakis, D. C. Olson, D. S. Ginley and G. Rumbles, *J. Am. Chem. Soc.*, 2009, **131**, 17726-17727.
12. A. Watt, E. Thomsen, P. Meredith and H. Rubinsztein-Dunlop, *Chem. Commun.*, 2004, **20**, 2334-2335.
13. H.-C. Liao, S.-Y. Chen and D.-M. Liu, *Macromolecules*, 2009, **42**, 6558-6563.
14. S. D. Oosterhout, M. M. Wienk, S. S. van Bavel, R. Thiedmann, L. Jan Anton Koster, J. Gilot, J. Loos, V. Schmidt and R. A. J. Janssen, *Nat. Mater.*, 2009, **8**, 818-824.
15. S. Dowland, T. Lutz, A. Ward, S. P. King, A. Sudlow, M. S. Hill, K. C. Molloy and S. A. Haque, *Adv. Mater.*, 2011, **23**, 2739-2744.
16. H.-C. Liao, C.-C. Lin, Y.-W. Chen, T.-C. Liu and S.-Y. Chen, *J. Mater. Chem.*, 2010, **20**, 5429-5435.
17. H. C. Leventis, S. P. King, A. Sudlow, M. S. Hill, K. C. Molloy and S. A. Haque, *Nano Lett.*, 2010, **10**, 1253-1258.
18. S. A. Dowland, L. X. Reynolds, A. MacLachlan, U. B. Cappel and S. A. Haque, *J. Mater. Chem. A*, 2013, **1**, 13896-13901.
19. W.-P. Liao and J.-J. Wu, *J. Phys. Chem. Lett.*, 2013, **4**, 1983-1988.
20. Y.-H. Lee, Y.-P. Lee, C.-J. Chiang, C. Shen, Y.-H. Chen, L. Wang and C.-A. Dai, *Macromolecules*, 2014, **47**, 5551-5557.
21. X. Wang, W. Song, B. Liu, G. Chen, D. Chen, C. Zhou and G. Shen, *Adv. Funct. Mater.*, 2013, **23**, 1202-1209.

22. Z. Li and X. Peng, *J. Am. Chem. Soc.*, 2011, **133**, 6578-6586.
23. B. Liu and E. S. Aydil, *J. Am. Chem. Soc.*, 2009, **131**, 3985-3990.
24. L. E. Greene, M. Law, B. D. Yuhas and P. Yang, *J. Phys. Chem. C*, 2007, **111**, 18451-18456.
25. P. Ravirajan, D. D. C. Bradley, J. Nelson, S. A. Haque, J. R. Durrant, H. J. P. Smit and J. M. Kroon, *Appl. Phys. Lett.*, 2005, **86**, 143101.
26. C. Y. Kwong, W. C. H. Choy, A. B. Djurišić, P. C. Chui, K. W. Cheng and W. K. Chan, *Nanotechnology*, 2004, **15**, 1156.
27. Y.-Y. Lin, T.-H. Chu, S.-S. Li, C.-H. Chuang, C.-H. Chang, W.-F. Su, C.-P. Chang, M.-W. Chu and C.-W. Chen, *J. Am. Chem. Soc.*, 2009, **131**, 3644-3649.
28. P. Ravirajan, S. A. Haque, J. R. Durrant, D. D. C. Bradley and J. Nelson, *Adv. Funct. Mater.*, 2005, **15**, 609-618.
29. K. Shankar, G. K. Mor, H. E. Prakasam, O. K. Varghese and C. A. Grimes, *Langmuir*, 2007, **23**, 12445-12449.
30. X. Chen and S. S. Mao, *Chem. Rev.*, 2007, **107**, 2891-2959.
31. Y. Wang, Y. He, Q. Lai and M. Fan, *Journal of Environmental Sciences*, 2014, **26**, 2139-2177.
32. B. O'Regan and M. Grätzel, *Nature*, 1991, **353**, 737-740.
33. H. Imai, H. Morimoto, A. Tominaga and H. Hirashima, *J. Sol-Gel Sci. Technol.*, 1997, **10**, 45-54.
34. H. Imai and H. Hirashima, *J. Am. Ceram. Soc.*, 1999, **82**, 2301-2304.
35. M. Langlet, A. Kim, M. Audier and J. M. Herrmann, *J. Sol-Gel Sci. Technol.*, 2002, **25**, 223-234.
36. M. Langlet, A. Kim, M. Audier, C. Guillard and J. M. Herrmann, *J. Mater. Sci.*, 2003, **38**, 3945-3953.
37. C.-H. Lu, W.-H. Wu and R. B. Kale, *J. Hazard. Mater.*, 2007, **147**, 213-218.
38. R. Miyakoshi, K. Shimono, A. Yokoyama and T. Yokozawa, *J. Am. Chem. Soc.*, 2006, **128**, 16012-16013.
39. R. Miyakoshi, A. Yokoyama and T. Yokozawa, *Chem. Lett.*, 2008, **37**, 1022-1023.
40. X. Guo, N. Zhou, S. J. Lou, J. Smith, D. B. Tice, J. W. Hennek, R. P. Ortiz, J. T. L. Navarrete, S. Li, J. Strzalka, L. X. Chen, R. P. H. Chang, A. Facchetti and T. J. Marks, *Nat. Photon*, 2013, **7**, 825-833.
41. W.-C. Chen, Y.-H. Lee, C.-Y. Chen, K.-C. Kau, L.-Y. Lin, C.-A. Dai, C.-G. Wu, K.-C. Ho, J.-K. Wang and L. Wang, *ACS Nano*, 2014, **8**, 1254-1262.
42. S. Lattante, *Electronics*, 2014, **3**, 132.
43. C. H. Sun, X. H. Yang, J. S. Chen, Z. Li, X. W. Lou, C. Li, S. C. Smith, G. Q. Lu and H. G. Yang, *Chem. Commun.*, 2010, **46**, 6129-6131.
44. H. G. Yang, C. H. Sun, S. Z. Qiao, J. Zou, G. Liu, S. C. Smith, H. M. Cheng and G. Q. Lu, *Nature*, 2008, **453**, 638-641.
45. H. Yin, Y. Wada, T. Kitamura, S. Kambe, S. Murasawa, H. Mori, T. Sakata and S. Yanagida, *J. Mater. Chem.*, 2001, **11**, 1694-1703.

46. D. A. H. Hanaor, I. Chironi, I. Karatchevtseva, G. Triani and C. C. Sorrell, *Adv. Appl. Ceram.*, 2012, **111**, 149-158.
47. S.-S. Li, C.-P. Chang, C.-C. Lin, Y.-Y. Lin, C.-H. Chang, J.-R. Yang, M.-W. Chu and C.-W. Chen, *J. Am. Chem. Soc.*, 2011, **133**, 11614-11620.
48. J. A. Labastide, M. Baghgar, A. McKenna and M. D. Barnes, *J. Phys. Chem. C*, 2012, **116**, 23803-23811.
49. E. T. Niles, J. D. Roehling, H. Yamagata, A. J. Wise, F. C. Spano, A. J. Moulé and J. K. Grey, *J. Phys. Chem. Lett.*, 2012, **3**, 259-263.
50. M. Baghgar, J. A. Labastide, F. Bokel, R. C. Hayward and M. D. Barnes, *J. Phys. Chem. C*, 2014, **118**, 2229-2235.
51. T. W. Holcombe, C. H. Woo, D. F. J. Kavulak, B. C. Thompson and J. M. J. Fréchet, *J. Am. Chem. Soc.*, 2009, **131**, 14160-14161.
52. J. Wu, G. Yue, Y. Xiao, J. Lin, M. Huang, Z. Lan, Q. Tang, Y. Huang, L. Fan, S. Yin and T. Sato, *Sci. Rep.*, 2013, **3**, 1283.

Graphical abstract: